Available online at www.sciencedirect.com

ScienceDirect

Journal of Nuclear Materials 374 (2008) 147–157

journal of nuclear materials

www.elsevier.com/locate/jnucmat

Helium release and microstructural changes in $Er(D,T)_{2-x}{}^3He_x$ films

C.S. Snow [a,*], L.N. Brewer [a], D.S. Gelles [b], M.A. Rodriguez [a], P.G. Kotula [a],
J.C. Banks [a], M.A. Mangan [a], J.F. Browning [a]

[a] *Sandia National Laboratories, Albuquerque, NM 87185, United States*
[b] *Pacific Northwest National Laboratory, Richland, WA 99352, United States*

Received 29 January 2007; accepted 17 July 2007

Abstract

$Er(D,T)_{2-x}{}^3He_x$, erbium di-tritide, films of thicknesses 500 nm, 400 nm, 300 nm, 200 nm, and 100 nm were grown and analyzed by transmission electron microscopy, X-ray diffraction, and ion beam analysis to determine variations in film micro-structure as a function of film thickness and age, due to the time-dependent build-up of ^3He in the film from the radioactive decay of tritium. Several interesting features were observed: One, the amount of helium released as a function of film thickness is relatively constant. This suggests that the helium is being released only from the near surface region and that the helium is not diffusing to the surface from the bulk of the film. Two, lenticular helium bubbles are observed as a result of the radioactive decay of tritium into ^3He. These bubbles grow along the [1 1 1] crystallographic direction. Three, a helium bubble free zone, or 'denuded zone' is observed near the surface. The size of this region is independent of film thickness. Four, an analysis of secondary diffraction spots in the Transmission Electron Microscopy study indicate that small erbium oxide precipitates, 5–10 nm in size, exist throughout the film. Further, all of the films had large erbium oxide inclusions, in many cases these inclusions span the depth of the film.
Published by Elsevier B.V.

PACS: 81.40.Wx; 81.65.Mq; 89.30.Gg; 89.30.Jj; 61.10.Nz; 68.08.De

1. Introduction

Inert gases, such as helium and argon, can be introduced into a metal matrix in a wide variety of methods and in many applications [1]. For example, helium is found to accumulate in metal tritides when the tritium decays into ^3He [2], is produced in nuclear devices due to irradiation [3], or can be implanted into materials [4]. In many of these cases, the build up of inert gases in the metal matrix is detrimental to the application because it degrades the mechanical properties of the material [5]. It has long been established that inert gases in a metal matrix at sufficient densities will aggregate to form bubbles. How these inert gas bubbles form, grow, and interact is an active area of theoretical and experimental research along with their effect on a metal matrix's electrical, magnetic, mechanical, and structural properties.

There are two methods in which inert gases can enter a metal matrix, a 'gentle' method through the radioactive decay of tritium, and a 'violent' method through either implantation or nuclear reaction. The 'violent' methods are what occur in most applications with the obvious exception of tritium storage. The two methods of introducing inert gases give different micro-structural environments due to vacancies, induced dislocations and defects, etc., and their study gives different information about the behavior of inert gases in solids. In this study we focus on the 'gentle' method of tritium decay for the following reasons: the helium is introduced in a well controlled and understood process; the helium spatial distribution is uniform as long as the tritium is uniformly distributed; the helium is introduced without significant damage to the metal lattice, whereas implantation or nuclear reaction produces

---

[*] Corresponding author.
E-mail address: cssnow@sandia.gov (C.S. Snow).

0022-3115/$ - see front matter Published by Elsevier B.V.
doi:10.1016/j.jnucmat.2007.07.021

significant metal lattice damage; the metal hydride is thermodynamically stable; and samples of various configuration and size can be produced. In order to model and understand the behavior of inert gases, like helium, in materials one needs to understand the films micro-structure. This paper will focus on the effect of time and film thickness on the micro-structure, helium accumulation, and the amount of helium released from $Er(D,T)_{2-x}{}^{3}He_x$ films.

A large body of theoretical work has been done to model and understand inert gas bubble formation in materials. Since in most applications the inert gas enters via one of the 'violent' methods, most of the theoretical studies have dealt with helium introduced by implantation or nuclear reaction [18,19]. While much of the theoretical work can be modified to capture the important physics of both the implanted and tritium methods, there are several important differences where the existing models may not be applicable: First, the helium concentrations in the tritium materials cover a much larger range, from 0.01 to 0.40 He/Metal ratios whereas the ratio in implanted materials ranges up to a few thousand appm, or a He/M ratio of about 0.01–0.001 He/M. Second, the nature and origin of dislocations and defects is different. The introduction of helium via implantation or nuclear reaction causes a large number of defects. For example, helium implantation into SiC displaces 60–73 atoms per implanted helium atom [18]. While in tritides the recoil energy of the helium atom produced via tritium decay is too low to cause any lattice damage. Finally, the helium production rate in implanted materials typically falls between 1 and 100 appm He/h, while in metal tritides the rate starts out at $\sim$10 appm He/h for materials like ErT_2 and decreases exponentially.

Much work has been done on transition and rare-earth metal hydrides [6]. Vajda has written an excellent review of rare-earth metal hydrides in the RH_{2+x} phase [7]. ErH_{2+x} forms in the CaF_2 structure, shown in Fig. 1, (Space Group $Fm\bar{3}m$, # 225) over a wide composition range from approximately $-0.20 < x < 0.20$ [8]. Yttrium, Scandium, and Titanium di-hydrides also form in the CaF_2 crystal structure. The CaF_2 unit cell contains four Erbium atoms forming an FCC lattice with the eight hydrogen occupying the tetrahedral sites. In the perfect crystal the octahedral sites are unoccupied although measurements on similar metallic dihydrides have shown that a small fraction of octahedral sites are occupied even for $x = 0$ at $T = 300$ K [9]. The electrical properties of the ErH_{2+x} films also show dramatic changes with temperature and stoichiometry. The 300 K resistivity changes by a factor of ten by simply changing x from 0.07 to 0.091. Also, two metal-semiconductor transitions, a high-temperature one near 200 K and one at lower temperature, occur which are both profoundly effected by stoichiometry. Further, there is evidence that the excess hydrogen orders at low-temperatures [10,11].

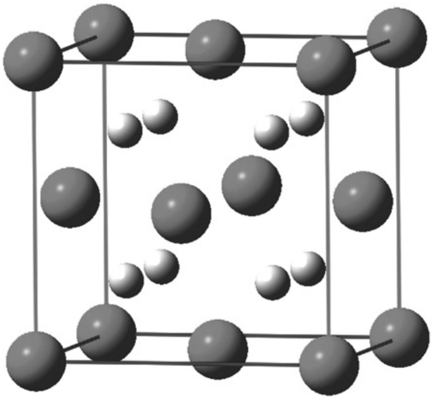
Fig. 1. CaF_2 FCC crystal structure of ErH_2, Space Group $Fm\bar{3}m$, # 225. The large grey spheres represent the Erbium atoms and the small white sphere represent the Hydrogen atoms.

The effects of helium accumulation in films of $Er(D,T)_2$ has been studied extensively over the past 30 years. Experimentally, it was found that most of the helium generated by the decay of tritium into ^3He was retained in the film and only a small fraction, 0.1–0.01%, was released from the film [12]. Other measurements indicated that the helium released from the film was released in spurts of 10^{-15}–10^{-13}-mols [13]. Measurements of the amount of swelling of Erbium, Yttrium, Holmium, Titanium, and Scandium tritide films with age, i.e., amount of ^3He in the film, showed a near linear swelling rate with age with only the slope changing with different materials [14]. The authors used this evidence to suggest that helium was accumulating in bubbles in these films. A theoretical analysis of helium bubble formation looking at the energetics and formation kinetics of helium bubbles in metals was done by Trinkaus [15]. Evans also studied how bubbles interact and cause blistering of material surfaces. He proposed an inter-bubble fracture mechanism whereby the highly pressurized helium bubbles cause the material to fracture thus linking up two bubbles [16]. A later work by Cowgill took a rate equation approach to study helium bubble nucleation. In this model, he assumes that bubbles are nucleated by self-trapping and the effects of trapping at impurities or defects are ignored. Cowgill then solves a set of rate equations to determine atomic helium and helium bubble concentrations as a function of time and depth [17]. Cowgill's model makes several predictions: one, that most bubble nucleation occurs within the first several days of tritium entering the material. Two, that near the surface and grain boundaries that a region should exist that is void of bubbles. Third, that the helium released from the film is released from the near surface region, a few tens of Angstroms thick.

The purpose of this paper is to begin to shed light on the complicated micro-structure of rare-earth metal tritides so that more accurate, directly applicable models can be developed. This paper will proceed as follows: First, we will describe the important experimental procedures used to grow and tritide the films and how the samples were prepared for TEM analysis. Second, we will present the results and discussion on how film thickness and age influences sample morphology and helium release. Finally, we conclude with a discussion of the implications of these results on helium release models and other film properties.

2. Experimental procedures

2.1. Film growth and tritium loading

Erbium films were deposited by electron-beam evaporation onto rolled-molybdenum substrates to nominal thicknesses of 500 nm, 400 nm, 300 nm, 200 nm, and 100 nm. The substrate temperature during evaporation was 450 C and deposition occurred at a rate of 1 nm/sec. The erbium films were removed from the evaporator at ambient conditions and then placed in a special机 tritiding apparatus. The samples were brought to an elevated temperature and held there after which the sample was brought to the desired temperature to react with the hydrogen gases. The samples and deuterium/tritium gas mixtures were reacted at appropriate temperatures and pressures to produce a di-hydride with stoichiometry close to $Er(D,T)_{2.0}$. After the reaction was completed the gas was then removed from the chamber and the chamber was allowed to cool down to ambient conditions. The samples were then stored for a period in an inert atmosphere and sealed into a special UHV vacuum envelope. Interestingly, all of the tritided 400 nm films and some of the 300 nm films were observed to have delaminated from the molybdenum substrate upon opening the vacuum storage envelopes. The XRD measurements of film texture were only able to study the 500 nm, 200 nm, and 100 nm films while TEM images were obtained for all but the delaminated 400 nm films. It is believed that the 400 nm film delamination was due to a substrate contamination problem. Unfortunately, because of the radioactive nature of the samples further chemical analysis of the films and substrate was not possible.

2.2. Sample storage and helium measurements

The samples were stored in a sealed UHV vacuum envelope until they were to be studied by TEM or XRD. The vacuum envelope and sample were heated to above 300 C and evacuated for several hours in order create the UHV environment. To remove the samples from the sealed UHV vacuum envelopes and to measure the amount of helium evolved from the metal tritide films, the vacuum envelopes were attached to a Finnegan Mass Spectrometer and punctured. This was done so that the quantity and type of gases in the envelope could be determined. The helium release measurements reported on in Section 3.5 were obtained in this manner.

2.3. TEM preparation and analysis

Cross-sectional TEM samples were prepared using conventional techniques. Sections from the $Er(D,T)_{2-x}{}^{3}He_{x}$ samples were cut using a low speed diamond saw. These sections (~2 mm wide by 1 cm long) were inserted into a 3 mm outer diameter, molybdenum tube along with molybdenum spacers to fill as much of the tube volume as possible. The tube was then vacuum impregnated with G2 (Gatan Inc.) epoxy and cured on a hot plate at 100 C for 5 min. After the curing process, the tube was sectioned into cylinders 3 mm in diameter and ~0.5 mm in thickness. These cylinders were mechanically ground and polished to a 1 μm finish on one side and down to a sample thickness of less than 100 μm. The samples were then dimpled on the opposite side to a thickness of approximately 20 μm. Finally, the samples were thinned to transparency using a low angle (4°), low energy (1–4 keV) Ar ion milling in a Gatan PIPS.

TEM analysis was performed using a JEOL 2000FX 200 keV TEM permanently installed in a tritium compatible facility. EDX spectra were collected using a Thermo-Noran UTW-Si(Li) detector system. Bright field images of the He bubbles were collected by tilting the sample to a $\langle 110 \rangle$ zone axis and then further tilting to a related two-beam condition, exciting the $g = \{111\}$ reflection. To calculate the volume density of bubbles required measurement of the sample thickness. The thickness of the sample was determined by collecting stereo-pairs of images and then using a stereo-imager to measure the thickness.

3. Results and discussion

3.1. Columnar grains and texture

Fig. 2 shows a TEM micrograph of the 500 nm and 100 nm films. It is clear from these images that the $Er(D,T)_{2-x}{}^{3}He_{x}$ films exhibit columnar grains. Savaloni and Player performed a detailed study of the growth of 600 nm thick erbium metal films on molybdenum [20]. They used the zone model developed by Grovenor et al. to describe the effect of substrate temperature and deposition rate on film microstructure [21]. For the conditions of 450 °C substrate temperature and 1 nm/s deposition rate, the erbium films in this study should fall in Zone II, or the columnar growth zone. Apparently, the effect of hydriding the erbium metal films does not impact this aspect of the microstructure. A detailed study of changes of grain size and other microstructural effects upon hydriding has been concluded and will be the topic of a future publication.

Fig. 3 shows the θ–2θ X-ray diffraction scans for the 500 nm, 200 nm, and 100 nm thick films. The inset shows the full pattern including the molybdenum substrate peaks. All data has been normalized to the intensity of the molybdenum (200) reflections so that a direct comparison could be made. Several interesting points become apparent; first, the $Er(D,T)_{2-x}$-(111) peak systematically decreases with decreasing film thickness; second, the Er_2O_3-(222) reflection peak increases with decreasing film thickness and is asymmetric. This point will be discussed in more detail

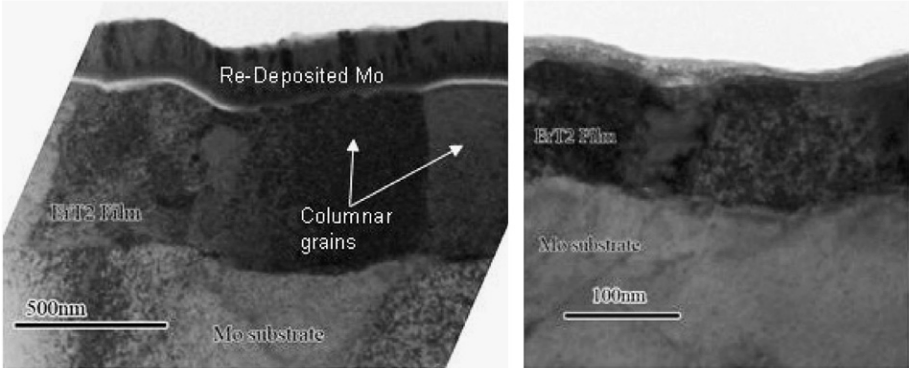

Fig. 2. TEM micrographs showing the columnar grain structure of the $Er(D,T)_{2-x}{}^3He_x$ films. The left micrograph is of the 500 nm film and the right is of the 100 nm film.

below; third, both the film and the molybdenum substrate are highly textured.

Fig. 4 shows the pole figures for molybdenum obtained on the 500 nm $Er(D,T)_{2-x}{}^3He_x$ film. The molybdenum substrate displays a strong (2 0 0) out-of-plane texture as illustrated by the strong central pole in the right picture of Fig. 4. Analysis of the molybdenum (1 1 0) pole shown in the left picture of Fig. 4 indicates that there is a biaxial-type texture in-plane which results in the nearly 4-fold symmetry of the (1 1 0) pole. This texture of the molybdenum substrate is not completely biaxial since the (1 1 0) poles tend to be elongated. This is likely a result of the rolling method used in the processing of the molybdenum metal substrates.

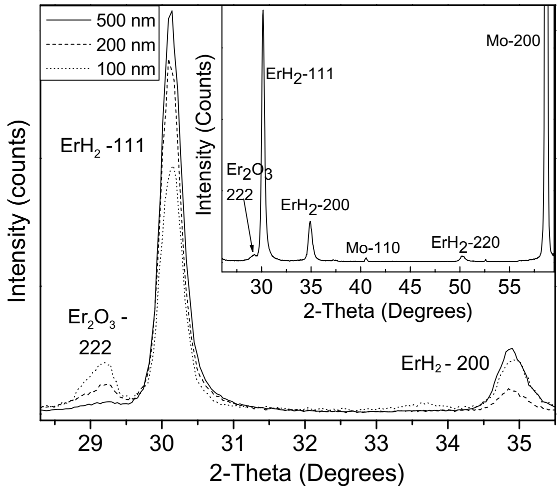

Fig. 3. XRD pattern of 500 nm, 200 nm, and 100 nm films showing specifically the $Er(D,T)_{2-x}$ peaks. The inset shows the full θ–2θ scan including the molybdenum substrate peaks.

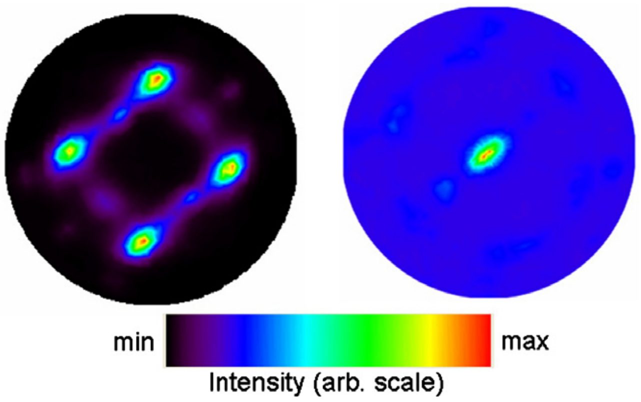

Fig. 4. Pole figures for the Molybdenum (1 1 0) (left) and (2 0 0) (right) peaks.

Fig. 5 shows the pole figures for the 500 nm, 200 nm, and 100 nm $Er(D,T)_{2-x}{}^3He_x$ films in the (1 1 1), (2 0 0), and (2 2 0) orientations. From these pictures one can see a strong (1 1 1) out-of-plane texture illustrated by the central pole in the $Er(D,T)_{2-x}{}^3He_x$ (1 1 1) pole figures; this is present in all of the film samples and is consistent with the θ–2θ scans. However, note that there is additional intensity in the form of a near 4-fold symmetry around the central (1 1 1) pole. These spots result from a secondary preferred orientation, namely a (2 0 0) out-of-plane preferred orientation that displays a bi-axial texture in-plane and appears to template from the molybdenum (1 1 0) grains. Note also in the $Er(D,T)_{2-x}{}^3He_x$ (2 0 0) pole figures that the (2 0 0) central poles do not quite superimpose on the very center of the pole figure, but actually show splitting of the poles to just off-center. This is most notable in the 500 nm thick film and is characterized as a clover-like formation in the center of the (2 0 0) pole figure. The $Er(D,T)_{2-x}{}^3He_x$ (2 0 0) pole figures also show intensity at higher χ tilts, which results from the (1 1 1) out-of-plane grains. When one considers this intensity, it appears that there is an approximate ring of intensity at approximately 54 degrees χ (the expected angle between the (2 0 0) and (1 1 1) planes) but the ring does not always show equal intensity all around the (2 0 0) pole figures. This is especially true for the 500 nm thick film. This film shows variability of counts around the ring. As the film gets thinner, the ring seems to become more apparent. The formation of a near continuous ring at 54 degrees χ would indicate an in-plane fiber texture for the (1 1 1) out-of-plane grains. Therefore, the thinner films display a more fiber-like in-plane texture, while the thicker films move toward a more biaxial texture that is dictated by the molybdenum substrate.

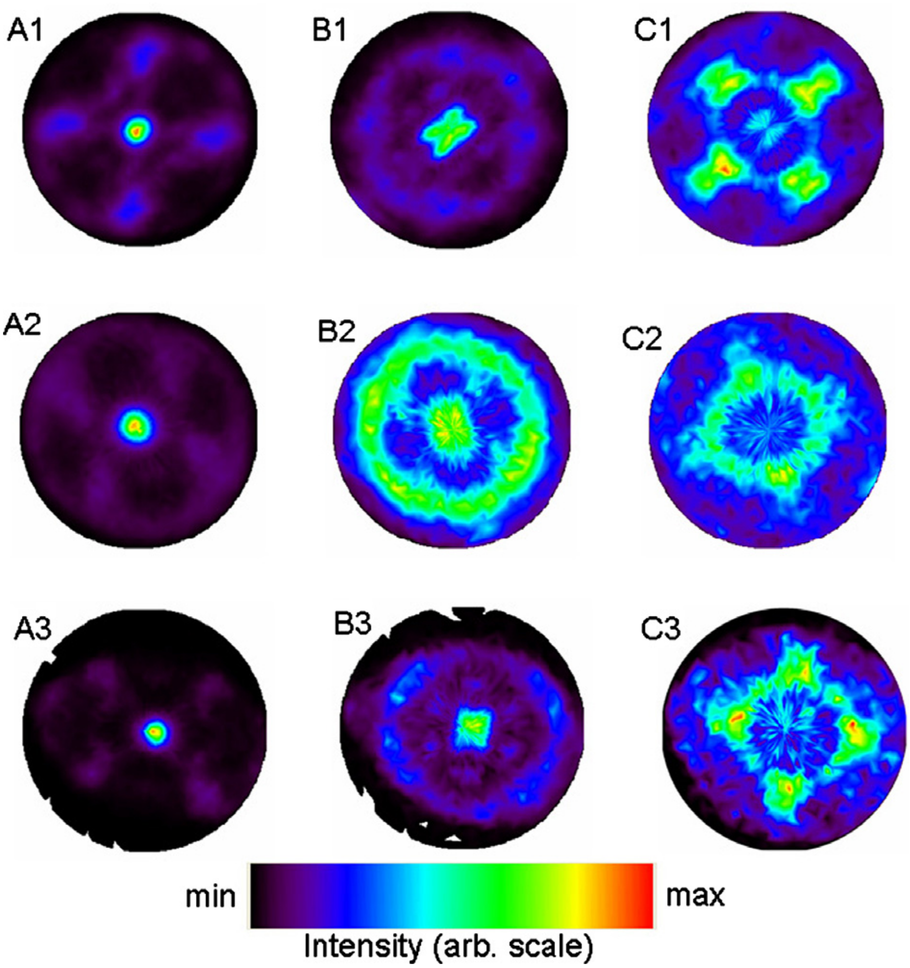

Fig. 5. Pole figures for the $Er(D,T)_{2-x}{}^3He_x$ films. Row 1 for the 500 nm, row 2 for the 200 nm, and row 3 for the 100 nm film. Column A is the pole figure for the (1 1 1) peak, column B for the (2 0 0) peak, and column C for the (2 2 0) peak.

Finally, Table 1 lists the measured lattice parameters of the $Er(D,T)_{2-x}{}^3He_x$ films. In all cases the molybdenum peaks were used as an internal standard. The $Er(D,T)_{2-x}{}^3He_x$ peaks were profile fit to assign accurate *d*-spacings for the films and a least-squares refinement for the peak positions was performed to obtain the *a*-axis value. A volume associated with the cell is also reported based on the measured lattice parameter. In some cases the error on the lattice parameter was large due to the lack of reflections present in the textured $Er(D,T)_{2+x}$ films. Within the error, these lattice parameters do not appear to be significantly different. Peak broadening in XRD can result from two influences, micro-strain and crystallite size. Due to the large crystallite sizes viewed from TEM, (see Fig. 2) on the order of 200–500 nm, nearly all of the peak broadening of the Erbium tritide results from micro-strain. This conclusion is reasonable considering the likelihood of micro-strain presence due to bubble formation/migration in the material.

Table 1
Lattice parameters measured from the $Er(D,T)_{2-x}{}^3He_x$ films

Film thickness (nm)	*a*-Axis (nm)	Cell volume (nm^3)
500	0.514(1)	0.136
200	0.5127(3)	0.135
100	0.5139(7)	0.136

3.2. Oxide layer thickness

Another interesting change that occurred in the films as a function of film thickness was a gradual increase in the native oxide layer, that oxide layer formed above the bubble denuded zone (see Section 3.7) shown in Fig. 12 and Fig. 13 as a result of reacting with an oxygen rich environment. Erbium and oxygen readily combine to form Er_2O_3 [22]. Ion beam analysis (IBA) measurements were performed to determine the native oxide thickness and the amount of oxygen residing in the 'bulk' of the film, these results are shown in Fig. 6. Interestingly, the native oxide thickness is seen to increase in thickness with thinner films. A similar result can be seen by analyzing the XRD Er_2O_3-(222) peaks in Fig. 3. Clearly the Er_2O_3-(222) peak is strongest in the 100 nm film. It is also interesting to note that the peak shape is skewed to the low 2θ side. This could indicate a variation of the lattice parameter of the Er_2O_3

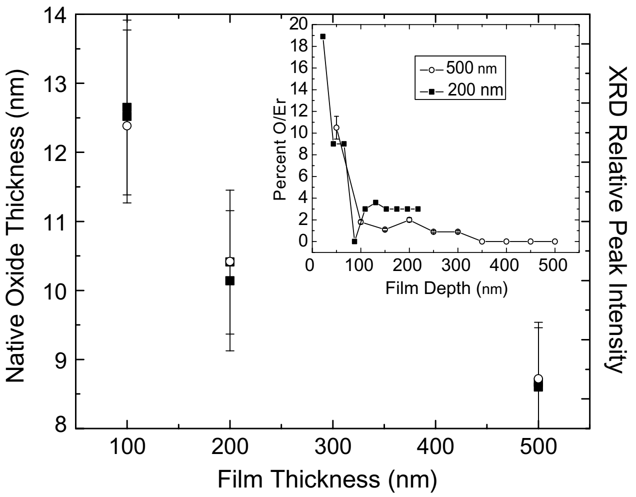

Fig. 6. Native oxide thickness as measured by IBA (■) is shown on the left axis. The oxide layer was modeled as Er_2O_3. The right axis shows the XRD peak intensity (○) of the Er_2O_3-222 peak intensity. The IBA measurements and the XRD results coincide exactly. The inset is a measure of the depth profile of the oxygen content as measured by IBA. 0 nm represents the surface and the depth is a measurement of distance from the surface. The error bars on the native oxide thickness and percent O/Er data points as determined by IBA is approximately 10% for each data point.

caused by a compositional gradient within the Er_2O_3 surface layer. Surface analysis studies using X-ray photoelectron spectroscopy (XPS) and sputter Auger Electron Spectroscopy (AES) have measured an oxygen gradient in the native Er_2O_3 oxide layer [23]. The inset of Fig. 6 shows a depth profile of oxygen in the films determined by IBA, a clear decrease of oxygen with film depth is seen indicating a compositional gradient of oxygen in the film. Elastic residual stress in the erbium oxide layer could also cause the peak asymmetry, although a rough estimate of the strain in the erbium hydride film made by comparing the molybdenum and erbium hydride thermal expansion coefficients suggest that it should be small, on the order of 2×10^{-5} [24]. Interestingly, the peak asymmetry could also be due to some additional phase forming. The idea of a finely dispersed oxide phase will be presented in more detail in Section 3.4 in association with analysis of a secondary spot pattern observed in the Selected Area Electron Diffraction (SAED) patterns taken with TEM. However, at this point it is not clear exactly what is causing the peak asymmetry, but it does occur in all three films.

A likely reason for the thicker oxide layer on the thinner samples is that there is roughly an equivalent partial pressure of oxygen in the film deposition chamber and when the thinner films are deposited more of the partial pressure is left un-reacted and hence free to react with the film surface. In this scenario the amount of oxygen in the 'bulk' of the films should be constant. While the data is far from conclusive, this trend is seen in the IBA analysis of the films in the inset of Fig. 6 where the percent of Oxygen/Erbium as a function of depth into the film is plotted. Beyond the near surface region the percent of Oxygen/Erbium is approximately 2–3%. These measurements were made by modeling the $Er(D,T)_{2-x}{}^3He_x$ films as ten separate slabs and fitting this slab model to the measurements. The discreteness of the approach and inherent resolution of the IBA technique produce the scatter, it is believed that oxygen is present in the 500 nm film beyond about 350 nm but that the amount of oxygen is probably 1% or so. The 100 nm film was too thin to be properly analyzed by this technique.

3.3. Oxide particles

Fig. 7 shows a TEM micrograph of a representative large inclusion in the $Er(D,T)_{2-x}{}^3He_x$ films. All films except the 500 nm thick film exhibit these large inclusions. The density of inclusions appears to be similar in all films, in fact, in every image and every sample prepared from the 300 nm, 200 nm, and 100 nm films an inclusion was found. It is not known why inclusions were not found in the 500 nm film. Given the large density of inclusions seen in the 300 nm, 200 nm, and 100 nm thick films, it is likely that the inclusions were simply missed in the sample selection and preparation process. Another interesting fact is that in virtually every image these inclusions were the same thickness as the films. Fig. 7(b) shows an energy dispersive X-ray (EDX) analysis spectrum taken from inside the inclusion compared to one taken from outside the particle in the film. The 0.5 keV oxygen peak is clearly larger inside the inclusion. Further, Selected Area Electron Diffraction (SAED) patterns taken on the inclusion are shown in Fig. 7(c) and (d) for two separate zone axis, the [1 1 0] and [211] of Er_2O_3 respectively. The arrows in the figures indicate where the expected spots should appear, in both images the expected Er_2O_3 zone axis match very well with the SAED patterns. These two facts clearly identify these inclusions as Er_2O_3. A study of the origin of these large oxide inclusions will be reported on in another publication.

3.4. Secondary spots

Careful examination of the diffraction patterns in Fig. 8 reveal a second set of diffraction spots that are not related to the erbium hydride fluorite structure itself. These spots appear in all of the samples that were examined and can be tracked as a function of tilt. The *d*-spacings associated with these secondary spots are 0.73 nm (g1) and 0.74 nm (g2). Dark field images using these diffraction spots (Fig. 8) show objects which are 5–10 nm in size, distributed through the grain.

The nearly ubiquitous presence of the secondary spots is most probably from incorporation of oxygen into the film. This oxygen appears to precipitate as fine particles (<10 nm) of Er_2O_3. The reflections g1 and g2 from Fig. 8 give *d*-spacings which are closest to the {1 1 0} spacing for Er_2O_3 (Table 2). These spots do not correspond well to any of the other phases listed in Table 2, including erbium metal, erbium tri-hydride, or erbium hydroxide.

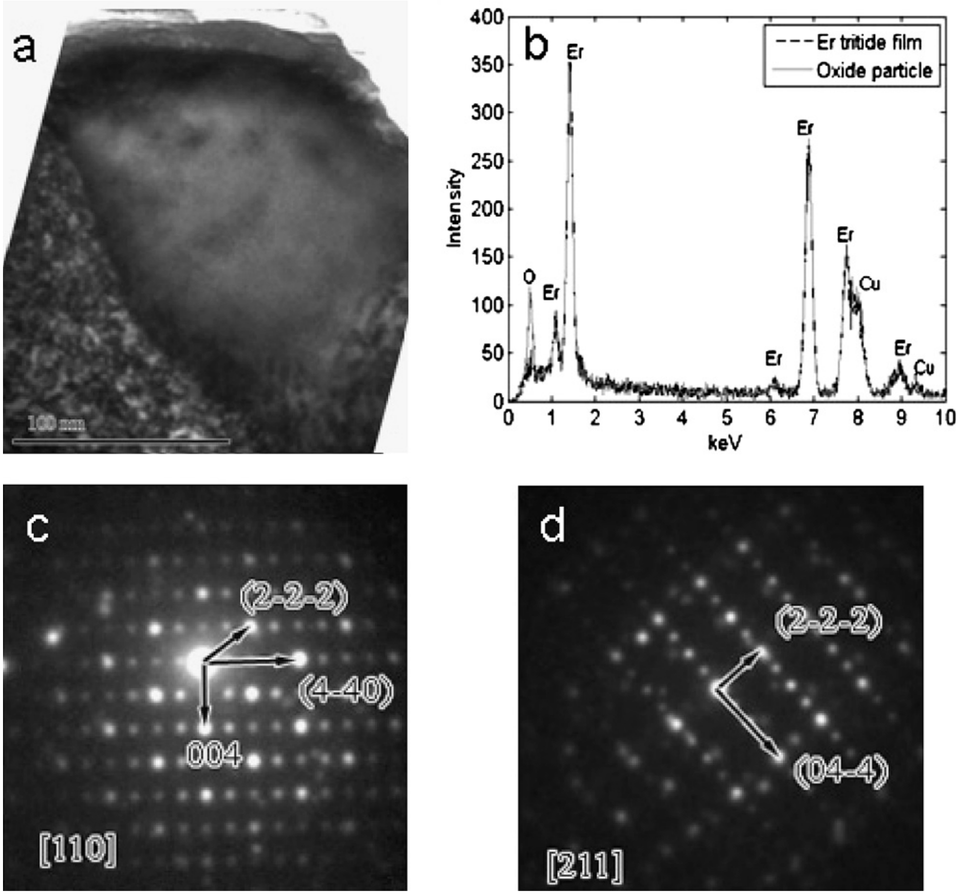

Fig. 7. (a) TEM Micrograph of large oxide particle in the 200 nm film; (b) compares two energy dispersive analysis (EDX) spectrum taken in the middle of the particle and outside the particle in the $Er(D,T)_{2-x}{}^3He_x$ film. The excess amount of oxygen is clearly present from the increased peak intensity of the approximately 0.5 keV oxygen peak; (c) and (d) are selected area diffraction patterns at different sample tilt angles. (c) Diffraction pattern along the [1 1 0] zone axis with the arrows showing the indexing to the Er_2O_3 unit cell. (d) Diffraction pattern along the [2 1 1] zone axis.

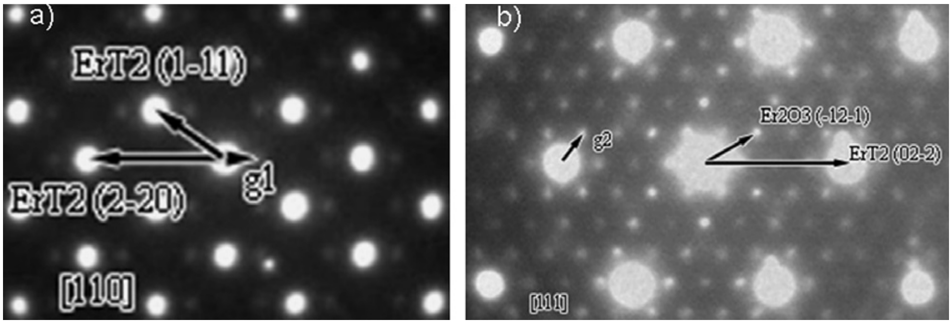

Fig. 8. SAED pattern showing primary spots from (a) the ⟨1 1 0⟩ and (b) the ⟨1 1 1⟩ zone axes of $Er(D,T)_2$ and secondary spots of unknown origin. The *d*-spacings associated with g1 and g2 are 0.73 nm and 0.74 nm, respectively.

Table 2
Comparison between measured *d*-spacing from secondary spots in SAED patterns and possible reflections from probable phases in the Er-H-O system

g	ErH_2 {*hkl*}/*d* (nm)	ErH_3 {*hkl*}/*d* (nm)	Er_2O_3 {*hkl*}/*d* (nm)	Er {*hkl*}/*d* (nm)	$Er(OH)_3$ {*hkl*}/*d* (nm)	ErO(OH) {*hkl*}/*d* (nm)
0.73 nm	{1 0 0}/0.515	{1 1 0}/0.541	{2 0 0}/0.5268	{1 0 0}/0.308	{1 0 0}/0.541	{1 0 0}/0.562
0.74 nm	{1 1 0}/0.364	{0 0 2}/0.326	{1 1 0}/0.745	{0 0 2}/0.280	{1 1 0}/0.312	{0 0 1}/0.406
	{1 1 1}/0.297		{2 2 2}/0.304			
			{2 2 0}/0.373			
	2[*]{1 1 0}/0.728					

---

[*] Multiplication.

Double diffraction is mostly likely responsible for the appearance of the g1 and g2 reflections. The Er_2O_3 {1 1 0} reflections that most closely correspond with g1 and g2 are not kinematically allowed in the Er_2O_3 space group (S.G. #206, Ia–3d); however, dynamical diffraction is common in electron diffraction patterns. The g1 reflection is clearly visible in Fig. 7(c) along the ⟨1 1 0⟩ axis of Er_2O_3. The appearance of the g1 reflection can result from double diffraction, such as the interaction between the (0 0 2) and the (1–1–2) reflections which results in the (1–10) reflection being visible (see Fig. 10 (Left)).

The diffraction pattern in Fig. 9, exhibits a completely aligned orientation relationship between $Er(D,T)_2$ and Er_2O_3; i.e. there is complete registry for all crystallographic directions for these two crystals. In Table 2, it can be seen that the $Er(D,T)_2$ and Er_2O_3 structures share similar d-spacings when multiplied by a factor of two; e.g. $Er(D,T)_2\text{-}d_{111} = 0.297$ nm and $Er_2O_3\text{-}d_{222} = 0.304$ nm, a difference of only 2.4%. In looking at Fig. 10 (Right), one can see that the {1 1 1} reflection for $Er(D,T)_2$ is nearly coincident with the position of the {2 2 2} reflection for Er_2O_3. Likewise, the {2 0 0} reflection for $Er(D,T)_2$ lies on top of the {4 0 0} reflection for $Er(D,T)_2$ and Er_2O_3. This close alignment of major reflections results in only the double diffraction, {1 1 0}, reflections from Er_2O_3 being distinct from the basic $Er(D,T)_2$ SAED pattern.

Compositional information from this system also supports the inclusion of oxygen into the $Er(D,T)_{2\text{-}x}{}^3He_x$ films, possibly as Er_2O_3. It is clear from the EDX measurements that there is a finite amount of oxygen incorporated into these nominally $Er(D,T)_{2\text{-}x}{}^3He_x$ films. Additionally, other studies have demonstrated the possibility for sub- and super-stoichiometric ErH_2 [8]. In the idealized fluorite lattice, all of the tetrahedral sites are filled. Any additional oxygen or hydrogen would most likely be incorporated into the octahedral sites in the lattice. Interestingly, the incorporation of oxygen onto every other octahedral site in $Er(D,T)_2$, results in a structure very similar to the Er_2O_3 structure.

3.5. ARF vs. thickness

The amount of helium released from the films was measured by puncturing the vacuum envelopes while they were connected to a Finnegan mass spectrometer as described above in Section 2.2. This technique measures the total amount of helium released and does not measure any time dependencies. A useful way of presenting this data is to ratio the amount of helium released to the amount of helium generated. The amount of helium generated is calculated after the fact by measuring the amount of tritium in the film taking into account the elapsed time since tritium was introduced in the sample. This ratio is commonly called the Average Release Fraction (ARF) and is defined as

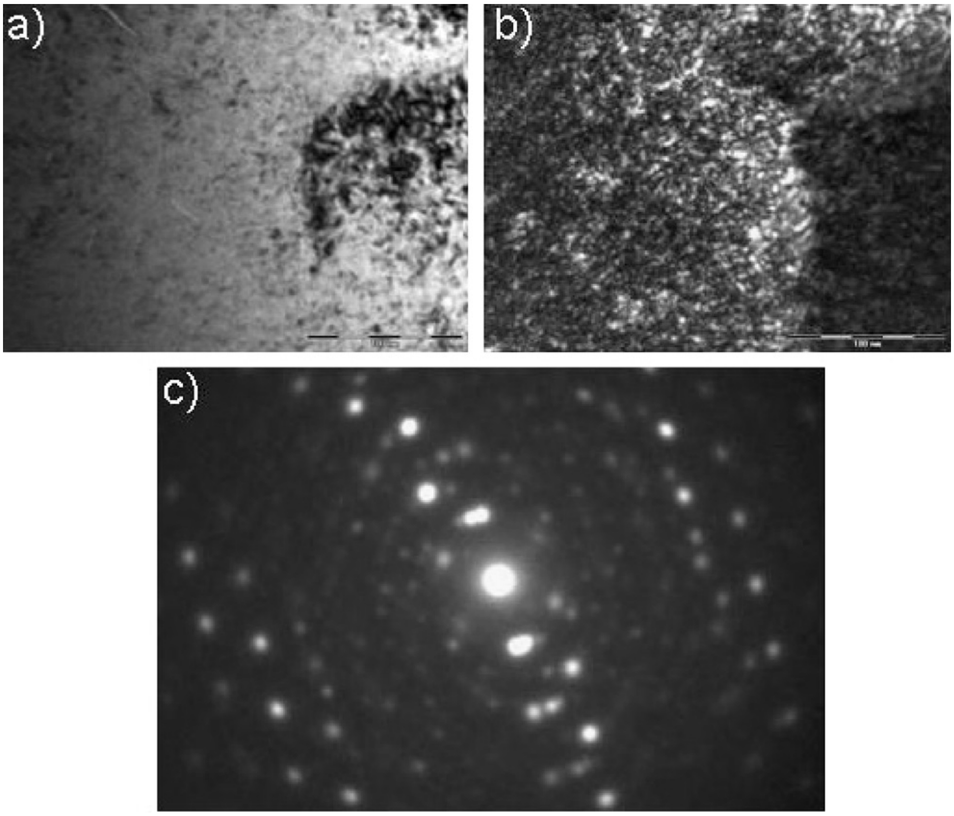

Fig. 9. (a) Bright field, (b) dark field image pair showing 5–10 nm objects corresponding to contrast from secondary spots in the (c) SAED pattern.

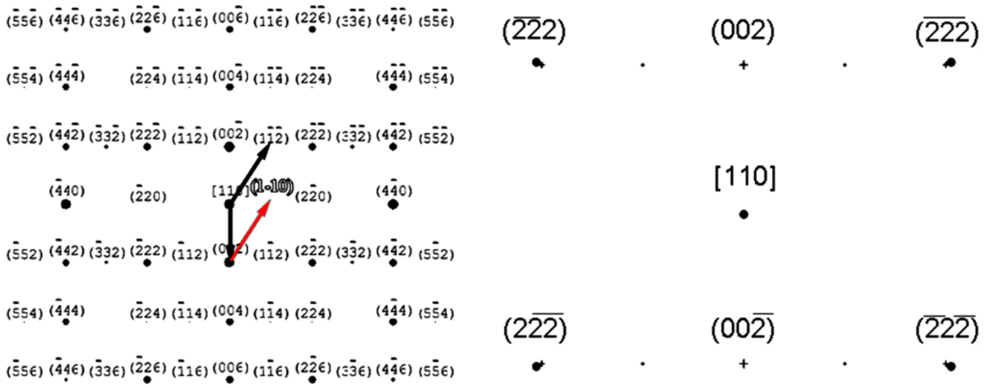

Fig. 10. (Left) Calculated SAED pattern for [1 1 0] zone axis of Er_2O_3. Red arrow shows double diffraction between (0 0 2) and (1–1–2), resulting in appearance of (1–10) reflection. (Right) Superimposed, calculated SAED patterns for ErD_2 and Er_2O_3. The black crosses and indices are for Er_2O_3 reflections while the circles are for ErD_2. Note the close overlap of the {2 2 2} reflections of Er_2O_3 and the {1 1 1} reflections of ErD_2.

$$\mathrm{ARF} = \frac{\text{Total Helium Released}}{\text{Total Helium Generated}}. \tag{1}$$

The results plotted as ARF vs. film thickness are shown in Fig. 11. The measurements were taken near the same He/M ratio of 0.02. The inset to Fig. 11 shows the total helium pressure inside the vacuum envelopes as a function of thickness. While significant scatter exists in the data, a trend of increasing ARF with decreasing film thickness is clearly present. Further, the partial pressure of ^{3}He released into the vacuum envelopes shows no significant trend, and varies by at most 0.07 mTorr. The fact that the total amount of ^{3}He released from the 100 nm film is not discernibly different than the 500 nm film, suggests that the helium being released is not diffusing from the full depth of the film. If the helium was diffusing to the surface from throughout the film, then the amount of helium released from the 500 nm film would be five times as large as that from the 100 nm. Instead, this data demonstrates that the helium that is released from the film originates effectively from a single layer, presumably near the top of the film ~0.2 nm thick. A simple analysis of a two layer system, where one layer releases helium into the vacuum envelope while another layer retains all of the helium, predicts that the ARF should vary inversely with thickness. The line in Fig. 11 is a fit of the ARF to the inverse of thickness. This model is a good fit to the data and appears to explain the major features of helium release from thin metal tritide films.

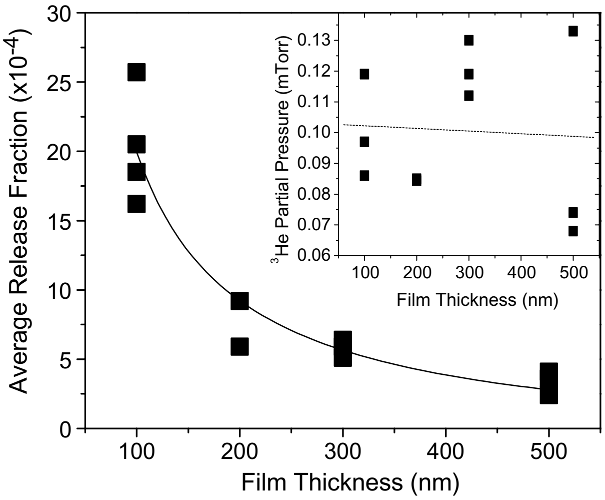

Fig. 11. Average Release Fraction (ARF) vs. film thickness. The solid line is a fit of the data to the equation 1/Thickness + Constant. The inset shows the total helium pressure vs. film thickness where the dashed line is a linear fit to the data.

3.6. Helium bubbles and bubble densities

Helium bubbles have been observed in a wide variety of materials, for example, He implanted in silicon [25], aged tritides like $VT_{0.15}$ [26] and $PdT_{0.2}$ [2], and irradiated structural materials [27]. It is interesting to note the differences in bubble shape that exists in the various systems. $PdT_{0.6}$ [28] exhibits spherical bubbles, while others, like TiT [2] and irradiated SiC are platelets. [18] Further, irradiated Si also exhibits platelet-type structures along the (1 0 0) planes [18].

Fig. 12 shows a TEM micrograph of helium bubbles in the 500 nm thick film. This image is representative of the other thicknesses in that all of the films exhibit platelet bubbles. Importantly, the bubbles are aligned along the [1 1 1] crystallographic axis. Platelet bubbles are caused by the elastic anisotropy of the system, [18] which for $Er(D,T)_{2.0}$ is readily apparent by examining the calcium fluorite structure shown in Fig. 1. Unfortunately, no experimental or theoretical calculations of the elastic constants of $Er(D,T)_{2.0}$ have been found to quantify the degree of elastic anisotropy. One last point, while not shown in this image, no increased helium bubble accumulation was observed on grain boundaries.

Table 3 shows the measured bubble sizes and volume densities as a function of thickness. The measured bubble densities were consistent with other measurements on PdT [28] but do not strongly correlate with film thickness (see Table 3). Due to the small number of samples and

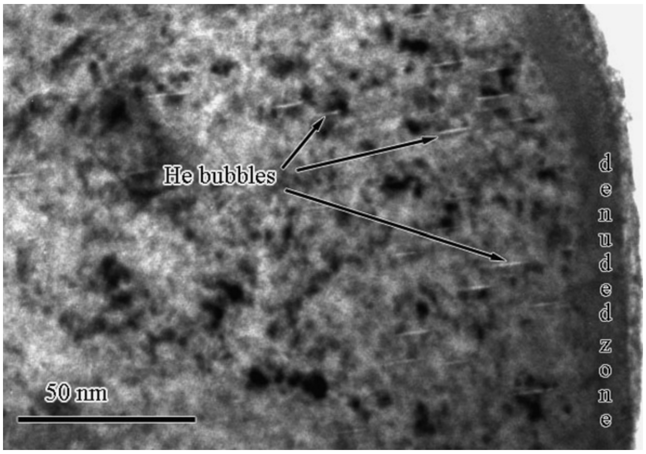

Fig. 12. TEM micrograph of the 500 nm thick film showing the lenticular bubbles and bubble denuded zone (to be discussed below in Section 3.7).

Table 3
Measurement of ^{3}He bubble size and density as a function of film thickness

Film thickness (nm)	He/M	Bubble diameter (nm)	Volume density ($\sharp/m^3$)
500	0.053	8.3 ± 0.9	2.9×10^{23}
300	0.06	15.4 ± 7.2	0.97×10^{23}
200	0.048	12.3 ± 4.9	3.2×10^{23}
100	0.053	3.6 ± 0.8	9.1×10^{23}

fields of view (one sample for each thickness, 2–3 fields of view for each sample), a definitive correlation is not possible. The number presented represents a measurement times a factor of four to account for the four {1 1 1} variants possible in any given field of view. This multiplication does require the assumption that the density of ^{3}He bubbles across {1 1 1} variants is uniform, but there is no physical reason for assuming a non-uniform distribution.

3.7. Bubble free zone or ‘Denuded zone’

An interesting feature of all of the Er(D,T)$_2$ films is the presence of a surface region void of observable helium bubbles. This feature can be seen in Figs. 12 and 13. This bubble free zone has been termed a ‘denuded zone’ [17] or ‘depleted zone’ [18] in reference to its absence of bubbles. It should be emphasized that it is not known if small, undetectable bubbles exist inside this zone or if all the helium in the region is atomic helium. The thickness of the denuded zone did not vary significantly with film thickness but rather stayed rather constant at ~15 nm. Some films had more clearly observed denuded zones while others were more difficult to detect due to the contrast of the image.

The origin of this bubble free zone can be understood by assuming that most of the helium created in this region diffuses to the surface creating a reduced bubble density [18,19]. However, if we assume that all of the helium created within this region actually escapes to the atmosphere the resulting ARF for the 500 nm film would be 0.03 while the observed ARF is 0.002. One possible explanation for this factor of ten discrepancy is that the bubble free region has a high concentration of atomic helium.

4. Impact on helium release/retention models

Several important features of real rare earth metal tritide films have been demonstrated in this paper that need to be incorporated into future models of helium release/retention. One, at least for erbium films, a significant amount of oxygen becomes incorporated into the film as large oxide inclusions and as finely dispersed oxide precipitates. Models of helium release from erbium tritide films, and probably many other rare earth films, will need to include the micro-structural effects associated with this additional oxide phase. Many open questions exist as to the effect of this oxide phase on helium release/retention. Do the oxygen clusters act as nucleation sites for helium

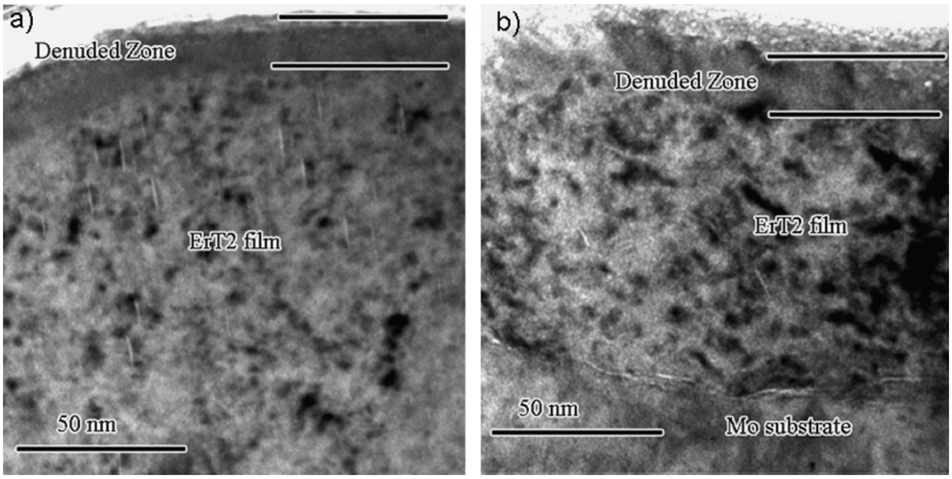

Fig. 13. Bubble free or ‘denuded zone’ of the (a) 500 nm and (b) 100 nm thick Er(D,T)$_2$ films.

atoms to begin to form bubbles? Do the oxygen clusters prevent the migration of helium throughout the lattice? A study by Schober and Trinkaus in $NbO_{0.015}T_{0.01\text{-}x}{}^3He_x$ suggests that oxygen acts as trapping sites for helium and suppresses ^3He bubble formation [29]. This effect though needs to be studied in more detail to determine the validity of this idea and/or the exact mechanisms involved. Two, the helium bubbles are not spherical but lenticular and they form along preferred lattice axis. Models of helium release via inter-bubble fracture will also need to include the directional dependence of helium bubbles in erbium tritide. Three, it was demonstrated that a bubble denuded zone exists. A characteristic length scale of ~15 nm was observed for all samples. The exact chemical nature of the denuded zone was not determined in this study but it was shown to include some oxygen. Models of helium release must predict the formation of a bubble denuded zone. Fourth, most of the helium released from the films appears to be coming from a near surface region given that the Average Helium Release Fraction (defined in Section 3.5) varies inversely with tritide film thickness.

In the introduction a brief discussion was given about a rate equation model proposed by Cowgill [17]. It is instructive to look at how our data compares to some of Cowgill's predictions. First, our films do demonstrate a 'denuded zone' as the rate equation model and other models suggest. An important difference though is the length scales, the rate equation model predicts a denuded zone of approximately 5-6 nm while we consistently observe a denuded zone of approximately 15 nm. This study was not able to determine what causes the denuded zone length scale. One obvious feature excluded from the rate equation model of Cowgill is actual micro-structural features of the films, this may be the cause for the discrepancy. Second, the rate equation model predicts that most of the helium that is released from the film is released from the near surface region. The data presented in Section 3.5 confirms this prediction. Importantly, we observe an ARF fraction that is smaller than predicted by the rate equation model. Again, this may be due to the rate equation model neglecting the actual micro-structural effects of the film. It is apparent that while the theoretical understanding of helium in metals has advanced significantly and many of the important features can now be calculated, it is now time to begin to study the effect of actual material micro-structures on helium behavior in metals.

Acknowledgements

The authors would like to acknowledge G. Bryant and C. Hill for the TEM sample preparation. This work was performed at and supported by Sandia National Laboratories. Sandia is a multiprogram laboratory operated by Sandia Corporation, a Lockheed Martin Company, for the United States Department of Energy under contract DE-AC04-94AL85000.

References

[1] D.E. Rimmer, A.H. Cottrell, Philos. Mag. 2 (1957) 1345.
[2] T. Schober, H. Trinkaus, in: S.E. Donnelly, J.H. Evans (Eds.), Fundamental Aspects of Inert Gases in Solids, Plenum, New York, 1991.
[3] H. Trinkaus, B.N. Singh, J. Nucl. Mater. 323 (2003) 229.
[4] S. Godey et al., Mater. Sci. Eng. B73 (2000) 54.
[5] H. Trinkaus, H. Ullmaier, J. Nucl. Mater. 212–215 (1994) 303.
[6] W.M. Mueller, J.P. Blackledge, G.G. Libowitz (Eds.), Metal Hydrides, Academic, 1968.
[7] P. Vajda, Chapter 137 in the Handbook on the Physics and Chemistry of Rare Earths, vol. 20, (1995)207.
[8] (a) C.E. Lundin, Trans. Metall. Soc. AIME 242 (1968) 1161;
(b) C.E. Lundin, Trans. Metall. Soc. AIME 242 (1968) 903.
[9] T.J. Udovic, Q. Huang, J.J. Rush, Phys. Rev. B. 61 (2000) 6611.
[10] P. Vajda, J. Alloy Compd 231 (1995) 170.
[11] P. Vajda, J.N. Daou, Phys. Rev. B. 49 (1994) 3275.
[12] D.J. Mitchell, R.C. Patrick, J. Vac. Sci. Technol. 19 (1981) 236.
[13] L.C. Beavis, W.J. Kass, J. Vac. Sci. Technol. 14 (1977) 509.
[14] L.C. Beavis, C.J. Miglionico, J. Less-Common Metals 27 (1972) 201.
[15] H. Trinkaus, Radiat. Eff. 78 (1983) 189–211.
[16] (a) J.H. Evans, J. Nucl. Mater. 68 (1977) 129;
(b) J.H. Evans, J. Nucl. Mater. 76–77 (1978) 228.
[17] D.F. Cowgill, Fusion Sci. Tech. 48 (2005) 539–544.
[18] J. Chen, P. Hung, H. Trinkaus, Phys. Rev. B 61 (2000) 12923–12931.
[19] H. Trinkaus, Radiat. Eff. 101 (1986) 91–107.
[20] H. Savaloni, M.A. Player, Vacuum 46 (1995) 167–179.
[21] C.R.M. Grovenor, H.T.G. Hentzell, D.A. Smith, Acta Metall 32 (1984) 773–781.
[22] N. Guerfi, O. Bourbia, S. Achour, Mater. Sci. Forum. 480&481 (2005) 193–196.
[23] C.R. Tewell, S.H. King, Appl. Surf. Sci. 253 (2006) 2597–2602.
[24] J.E. Bonnet, J.N. Daou, J. Appl. Phys. 48 (1977) 964–968.
[25] R. Siegele et al., Appl. Phys. Lett. 66 (1995) 1319–1321.
[26] T. Schober, R. Lasser, W. Jager, G.J. Thomas, J. Nucl. Mater. 122 & 123 (1984) 571–575.
[27] H. Trinkaus, H. Ullmaier, J. Nucl. Mater. 155–157 (1988) 148–155.
[28] G.J. Thomas, J.M. Mintz, J. Nucl. Mater. 116 (1983) 336–338.
[29] T. Schober, H. Trinkaus, Z. Phys. Chem. 183 (1994) 473–477.